Advances in Science and Technology Research Journal

Advances in Science and Technology Research Journal 2024, 18(1), 10–25
https://doi.org/10.12913/22998624/175377
ISSN 2299-8624, License CC-BY 4.0

Received: 2023.10.31
Accepted: 2023.12.17
Published: 2024.01.15

Effect of Friction on Buckling Behavior in Shallow Spherical to Hemispherical Shells in Contact with Rigid Boundaries under Uniform External Pressure

Xuan Cuong Nguyen[1,2], Yoshio Arai[3*], Wakako Araki[4]

[1] Division of Mechanical Engineering and Science, Saitama University, 255, Shimo-ookubo, Sakura-ku, Saitama, 338-8570, Japan

[2] Faculty of Mechanical Engineering, Hanoi University of Civil Engineering, 55, Giai Phong Road, Hai Ba Trung District, Hanoi, 100000, Vietnam

[3] Division of Mechanical Engineering and Science, Saitama University, 255, Shimo-ookubo, Sakura-ku, Saitama, 338-8570, Japan

[4] Department of Mechanical Engineering, Tokyo Institute of Technology, 2-12-1, Ohokayama, Meguro-ku, Tokyo, 152-8550, Japan

* Corresponding author's e-mail: yarai@mail.saitama-u.ac.jp

ABSTRACT

This study investigates the influence of friction on the buckling behavior of thin, elastic, spherical shells under uniform external pressure. The study spans a range of geometric parameters, from shallow shells to hemispheres. Three different end-edge boundary conditions – clamped, hinged, and frictional ends – are considered across a wide range of friction coefficients using an axisymmetric model and nonlinear buckling analysis. The spherical shell becomes increasingly susceptible to buckling when the friction coefficient falls below the converged friction coefficient. A formula is developed to estimate this converged friction coefficient for each geometric parameter. Furthermore, a boundary separating the effects of friction on critical pressure into distinct regions is established, and equations predicting critical pressure within each region are provided. The study also finds that friction influences the buckling mode transition in the shells. Due to significant changes in the theta angle of the no-bending point with increasing geometric parameter and friction coefficient, buckling mode transitions occur at lower friction coefficients in wider spherical shells. These findings provide valuable insights into the intricate interplay between geometric parameter, friction, and buckling behavior in shells. In practical applications, this study can be used to assess and enhance the safety and reliability of spherical shells.

Keywords: buckling mode, buckling mode transition, friction effect, nonlinear buckling, spherical shells.

INTRODUCTION

The critical buckling pressure of a spherical shell under uniform external pressure was first derived by Zoelly [1] based on linear shell theory:

$$p_0 = \frac{2E}{\sqrt{3(1-\upsilon^2)}}\left(\frac{t}{R}\right)^2 \quad (1)$$

where: t – the thickness, R – the radius, E and υ – represent Young's modulus and Poisson's ratio, respectively.

Equation 1 is applicable to a perfectly spherical shell. Extensive reviews and explanations of both experimental and theoretical results concerning the buckling behavior of complete spherical shells and spherical caps have been provided [2].

More recently, Pan et al. [3] proposed a novel empirical formula to determine the ultimate strength of titanium alloy spherical pressure hulls, which was subsequently validated through experimental testing [4]. The presented experimental, analytical, and numerical results on the buckling behaviors of spherical shells under uniform external pressure show excellent agreement [5]. Wagner et al. [6] carried out an exhaustive literature review and compiled approximately 700 experimental results of critical pressure in spherical shells to propose new shell-design approaches that are both time-efficient and cost-effective.

The buckling behavior of shallow spherical shells under uniform external pressure has received significant attention [7-28]. Buckling results are often presented in relation to a non-dimensional parameter known as the geometric parameter ρ, defined as

$$\rho = [6(-\upsilon^2)]^{\frac{1}{2}} \left(\frac{\beta^2 R}{t}\right) \tag{2}$$

where: β – the semi-angle of the shell opening.

One factor influencing the buckling response of shallow spherical shells is the end-edge boundary condition. The two most common boundary conditions studied are clamped and hinged ends, both of which play a crucial role in determining the buckling characteristics of the shells. Experiments on the buckling pressures of deep spherical shells subjected to uniform external pressure with clamped ends were conducted by Kloppel and Jungbluth [29]. These results revealed significantly lower values compared to the linear critical pressure represented in Eq. (1). Krenzke and Kiernan [19, 30, 31] derived an empirical curve for the elastic buckling strength of nearly perfect deep spherical shells based on experimental collapse pressures of both shallow and deep shells. Additionally, Huang [32] used the Rayleigh–Ritz method in conjunction with a variational principle to numerically determine the buckling pressure of thin spherical shells across a wide range of geometric parameters; these results could also be extrapolated to deep spherical shells. Numerical analyses [33, 34] were also employed to ascertain the buckling pressure of deep spherical shells with clamped ends under uniform external pressure, aligning well with existing literature. In summary, key highlights from the studies on the buckling behavior of deep spherical shells under uniform external pressure are as follows:

- Most studies have primarily focused on the buckling pressure of spherical shells with a clamped end as the boundary condition for the end edge.
- Buckling strength is influenced by the boundary condition of the end edge. As this boundary condition approaches that of an ideal fixed end, the buckling pressure of the spherical shells increases.
- Numerical methods can be effective in solving the end-edge boundary conditions related to the nonlinear buckling response of deep spherical shells under uniform external pressure.

The popular method to obtain the buckling response of spherical shells is through experiments. Testing has been conducted on complete spherical shells [4-6], shallow spherical shells [23, 24, 28], and deep spherical shells [29-31], with detailed test procedures provided in these literatures. In addition to the experimental method, theoretical buckling results for these types of spherical shells have been thoroughly examined [2, 7, 12, 21, 33]. With advancements in computer technology and the refinement of finite element methods, numerical analyses have become increasingly reliable in investigating the buckling behavior of spherical shells [3, 5, 21, 27, 33, 34].

In our previous study [35], we examined the impact of friction at the end edge in contact with rigid walls on the buckling behavior of shallow spherical shells. The results revealed a substantial influence of friction on both the critical buckling pressure and buckling deformation. Building on these findings, the current study extends its focus to more complex scenarios involving deep spherical shells, aiming to provide a comprehensive understanding of the effects of friction on buckling performance. Given the widespread applications of spherical shells, and deep spherical shells in particular, it is crucial to account for the effects of friction on their buckling strength to ensure safety and reliability. The objective of this study is to provide a whole picture of the effect of friction on the buckling behavior of spherical shells. With this aim, the study predicts the critical buckling pressure and determines the buckling deformation for every given pair of values of friction coefficient and geometric parameter.

The current results demonstrate a significant impact of friction at the end edge on the buckling behavior of deep spherical shells. This effect is categorized into three distinct regions, and specific equations are provided for each region,

outlining the parameters and their boundaries to illustrate how friction influences the critical buckling pressure. Additionally, the influence of friction on buckling deformation is also indicated. An equation depicting the relationship between the friction coefficient and buckling mode transition has been derived. As a continuation of the previous study, the geometric parameter in this investigation starts with the maximum value used in the prior study and progresses until reaching a value corresponding to a hemisphere. Consequently, the estimating equations for critical pressure developed in this study are applicable across all geometric parameters and friction coefficients. Additionally, this study extends the analysis of buckling mode transitions to higher modes.

METHODOLOGY

In this study, we have performed a nonlinear buckling analysis using the finite element method to investigate the impact of friction at the end edge of spherical shells on buckling behavior under uniform external pressure.

Geometry and material properties

Figure 1 illustrates the schematic of the spherical shell. The shell has a thickness t of 0.05 mm and a radius of curvature R of 77.70 mm. To prevent concentrated stresses at the contact regions between the end edge and rigid walls, a rounded edge with a radius R_e of 1×10^{-3} mm is created at the shell's end edge. Figure 1 also outlines the boundary conditions for this simulation. The spherical shell is subjected to a uniform external pressure p acting on its outer surface. The end edge of the shell has three distinct types of boundary conditions, as shown in Figures 1a, 1b, and 1c, which are referred to as the frictional, clamped, and hinged ends, respectively. Under the frictional end condition, the end edge of the shell is supported by rigid walls. To explore the effect of friction on the shell's buckling behavior, a variable friction coefficient f is introduced in the contact regions. This friction coefficient ranges from $f = 0.0$ (representing a frictionless end) to $f = 2.0$ for each geometric parameter. The penalty formulation method is employed to incorporate this friction coefficient. The buckling behavior of shallow spherical shells within the geometric parameter range of 8.6–71.8 under the frictional end condition has been examined in our previous study [35]. The current study extends the parameter range to 71.8–8866.0, corresponding to a hemisphere. Figure 2 shows configurations of the spherical shell for three different geometric parameters. The shells used in this study are made of aluminum alloy AA6061-T6, and its mechanical properties are listed in Table 1. The buckling behavior of spherical shells can be influenced by different materials. However, in this case study, the shell is assumed to be an isotropic, homogeneous, and elastic material.

Numerical model and analysis

An axisymmetric model is created due to the symmetry of the structure. A four-node axisymmetric quadrilateral element (CAX4R) with reduced integration and hourglass control is employed to decrease computational time and improve convergence [36]. This type of element is

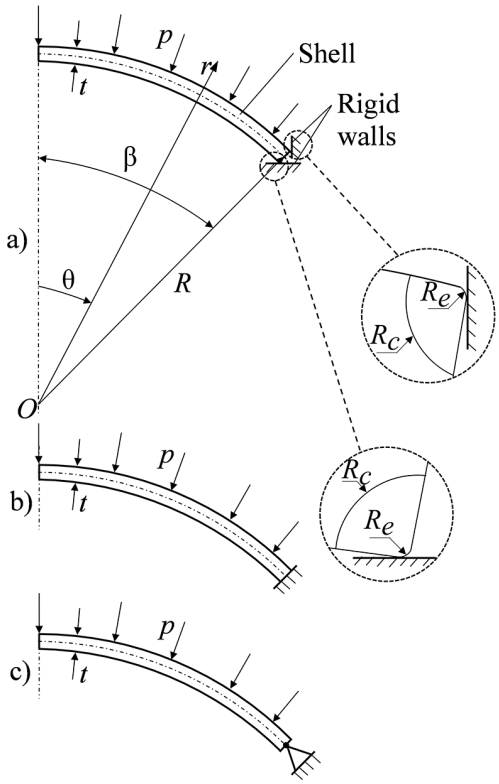

Fig. 1. Schematic of the spherical shell; (a) frictional end; (b) clamped end; (c) hinged end

Table 1. Mechanical properties of AA6061-T6

Young's modulus, E (MPa)	Poisson's ratio, v
68900	0.33

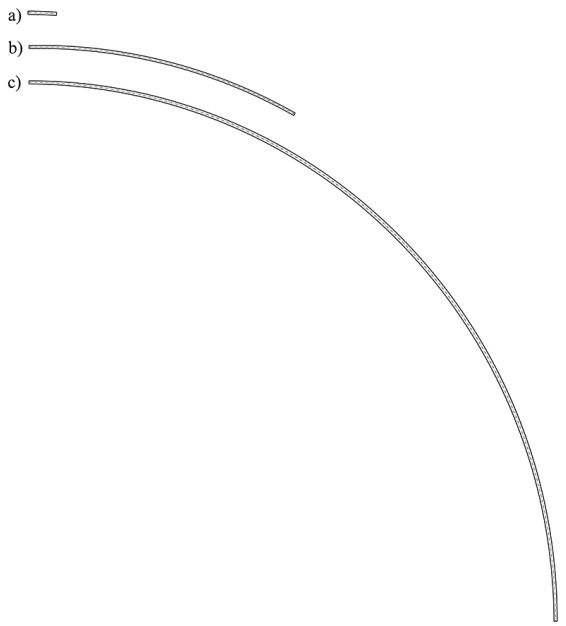

Fig. 2. Configuration of the spherical shells (ratio of semi-angle of shell opening 1:1 and ratio of thickness 5:1); (a) ρ = 8.6; (b) ρ = 985.1; c) ρ = 8866.0

suitable for analyzing structures with axisymmetric geometry subjected to axisymmetric loading. Furthermore, it can be used for complex nonlinear analyses involving contact and large deformations. Throughout the simulation, the spherical shell is considered to have a constant radius and uniform thickness, and initial imperfections are not accounted for. In the frictional-end condition, rigid walls are treated as fixed components. Under the clamped-end condition, all degrees of freedom at the shell's end edge are restrained. In the hinged-end condition, only the central point of the end edge is prevented from displacement, allowing the end edge to rotate freely.

The accuracy of the numerical simulation is significantly influenced by mesh size. However, an excessively fine mesh can result in increased computational time and cost [36, 37]. Therefore, a mesh convergence study is initially conducted to determine an appropriate mesh size. The common method for determining the suitable mesh size involves gradually increasing the number of elements or decreasing the size of the elements and then examining the results. Once the results stabilize, that mesh size can be regarded as suitable. In other words, the convergence of the results serves as a threshold for determining the suitable mesh size. Both the number of elements along the thickness N_t and the total number of elements N are examined across

Twelve different mesh sizes, detailed in Table 2, for the highest geometric parameter value of 8866.0. The objective is to compare based on the critical buckling pressure. A finer mesh density near the contact regions between the shell and rigid walls is necessary for the frictional end [38-40]. Thus, a mesh of size 0.08×10^{-3} mm surrounds the contact zone with a radius R_c of 0.01 mm, as shown in Figure 3. Mesh density increases gradually, ensuring finer mesh sizes are assigned closer to the contact regions. To maintain element continuity, intersection curves between coarse and fine mesh regions are meshed using an equal number of elements. This meshing approach for the contact regions is consistently applied across all configurations of spherical shells. To minimize the influence of the element aspect ratio, the element size is divided equally along both the thickness and polar directions.

The Riks algorithm [41-43] is used to trace the pressure–displacement curve in both the mesh refinement and nonlinear buckling analysis steps. The algorithm is known for its accuracy in predicting critical pressure and buckling deformation of spherical shells, whether considering friction [44-46] or not [6, 36, 47, 48]. Geometric nonlinearity is also incorporated in this analysis.

The critical pressure p_{cr} normalized using one of the fully perfect spherical shells is termed the relative critical pressure p_{cr}/p_0. The correlation between the relative critical pressure and the total number of elements is depicted in Figure 4. Mesh size significantly influences the critical buckling pressure of the spherical shell. A coarse mesh, corresponding to a small number of elements, decreases the critical pressure. The results stabilize once the mesh density reaches a certain threshold

Table 2. Number of elements along the thickness and the total number of elements corresponding to different mesh sizes

Mesh size ($\times10^{-3}$ mm)	25	12.5	8.3	6.3	5.0	4.2	3.6	3.2	2.8	2.5	2.0
N_t	2	4	6	8	10	12	14	16	18	20	25
N	9764	39056	87882	156224	244180	351624	478604	625104	791370	976720	1526125

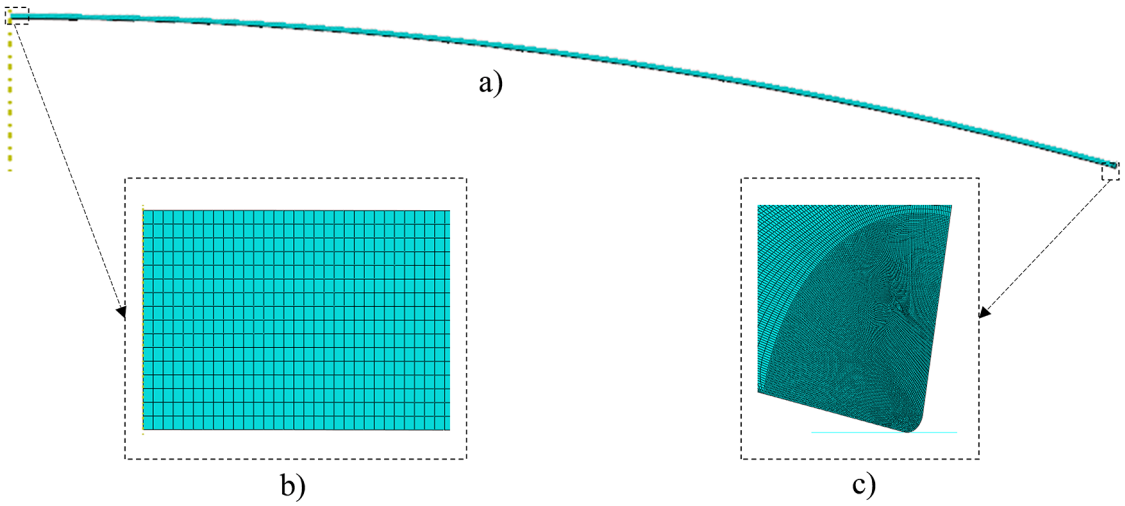

Fig. 3. Sample of mesh (ρ = 157.6); (a) overall mesh; (b) center part; (c) contact region

[36, 49]. Therefore, a mesh size of 2.5×10^{-3} mm, with 20 elements along the thickness, is deemed suitable for this analysis [46]. In the examined case of the geometric parameter of 8866.0, as presented in Figure 4, the chosen mesh corresponds to nearly one million elements. An example of a selected mesh in the central and contact regions is shown in Figure 3.

RESULTS AND DISCUSSION

Equilibrium paths, which present the relationship between external pressure and center displacement w_c, are shown in Figure 5 for clamped, hinged, and frictional ends. For clarity, this figure presents four specific geometric parameters: the smallest, highest, and two intermediate values, illustrating the buckling mode transition as the friction coefficient varies. In the frictional end scenario, the friction coefficient is gradually increased until the equilibrium curve converges with that of the clamped end. The critical buckling pressure, marked by circular points in Fig. 5, represents the pressure at which the shell loses its stability. The influence of friction on the pressure–displacement curve is particularly noticeable at low friction coefficients. In general, as the pressure increases, the displacement also exhibits a monotonic increase. However, as shown in Fig. 5b (with a geometric parameter of 157.6), at high friction coefficients, the displacement initially increases and then decreases with increasing pressure. These trends are consistent with observations made at smaller geometric parameters [35]. It can be observed in Figure 5 that under the same external pressure, the frictionless end exhibits the largest displacement. With an increase in the friction coefficient, this displacement gradually decreases and eventually converges with that observed in the clamped end. In contrast, the hinged end consistently shows the smallest displacement under the same external pressure, regardless of the geometric parameter.

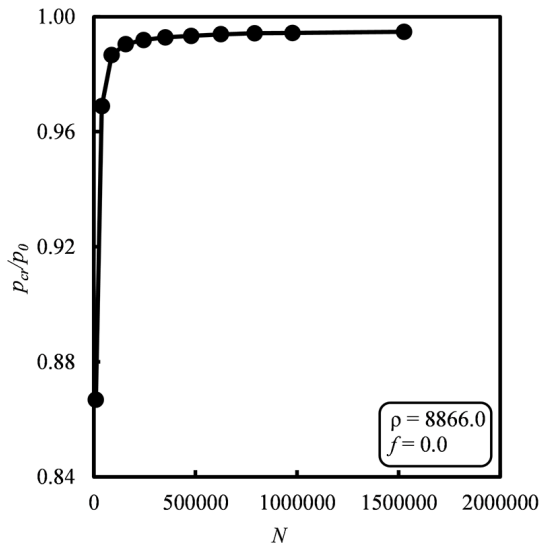

Fig. 4. Relationship between the relative critical pressure and the total number of elements

The critical pressures in Figure 5 are selected and plotted against the geometric parameter and friction coefficient, as illustrated in Figure 6a and 6b, respectively. In general, the critical pressure increases nonlinearly as either the geometric parameter or the friction coefficient increases.

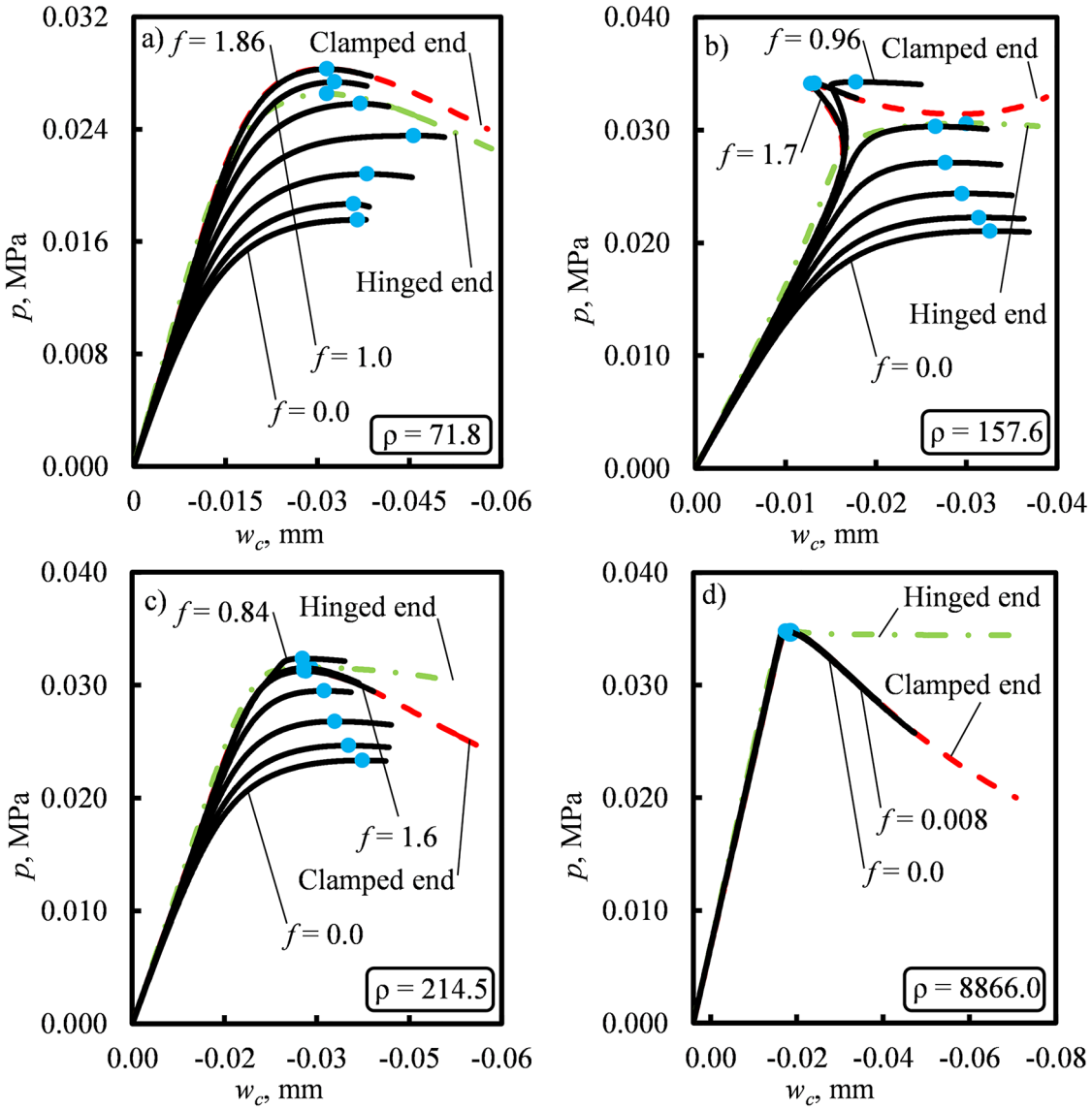

Fig. 5. Equilibrium paths for different geometric parameters with clamped, hinged, and frictional ends

Finally, this critical pressure converges with that of the clamped end. For each specific geometric parameter, this convergence occurs at a particular friction coefficient value, which will be examined in greater detail later. The relative critical pressure depicted in Figure 6, highlights significant differences among various end conditions. Generally, the clamped end exhibits the highest critical pressure, while the frictionless end displays the lowest. As the friction coefficient increases, the critical pressure nonlinearly increases, eventually converging with that of the clamped end. Despite its ability to rotate freely, the hinged end maintains a critical pressure higher than that of the frictionless end. Notably, the critical pressure for the clamped end in this simulation aligns with previous studies; these studies observed a fluctuation in critical pressure at low geometric parameters. As the geometric parameter increases, the critical pressure approaches that of a complete sphere, as indicated in Eq. 1 [15, 34, 50].

The equilibrium path and critical pressure in the frictional end converge with those in the clamped end as the friction coefficient increases, as shown in Figure 5 and 6. The friction coefficients at which the buckling behavior in the frictional end converges with that in the clamped end (referred to as the converged friction coefficient f_c) are determined and plotted against the geometric parameters, as illustrated in Figure 7. Convergence for narrow spherical shells occurs at higher friction coefficients. Moreover, the converged friction coefficient decreases nonlinearly as the geometric parameter increases.

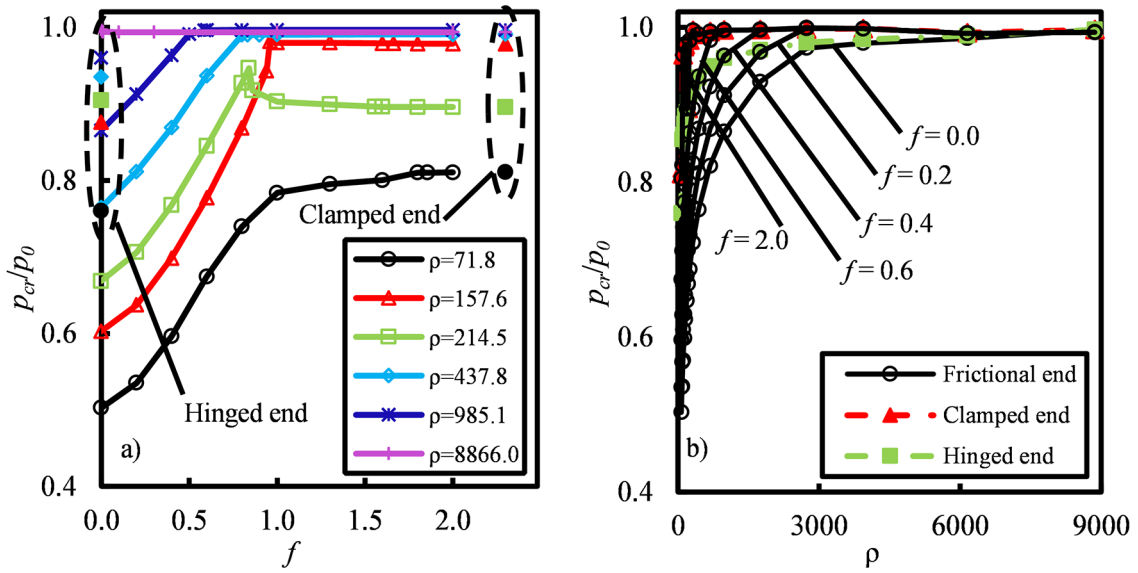

Fig. 6. (a) Relative critical pressure vs. friction coefficient for different geometric parameters and (b) relative critical pressure vs. geometric parameter for different end-edge boundary conditions

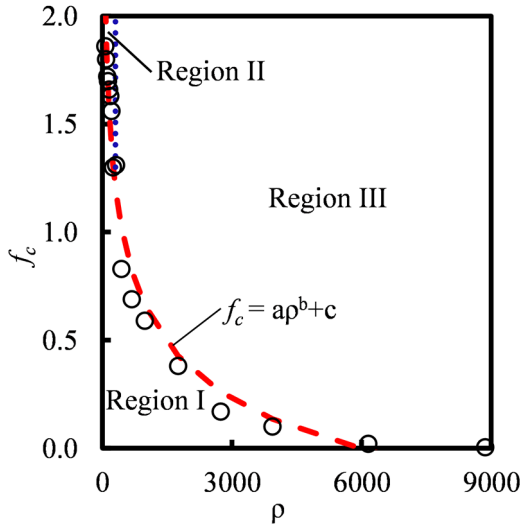

Fig. 7. Relationship between geometric parameter and converged friction coefficient

The formula for the converged friction coefficient is given by

$$f_c = a\rho^b + c \tag{3}$$

Equation 3 can be used to predict the converged friction coefficient from the geometric parameter with an RMSE of 0.12. The constants a, b, and c are provided in Table 3. As depicted in Figure 7, the impact of friction on the buckling behavior of spherical shells can be categorized into three distinct regions: region I, region II, and region III. Region I encompasses friction coefficient values that are smaller than the converged friction coefficient across all geometric parameters. In this region, changes in the friction coefficient have a substantial impact on the buckling behavior of the spherical shells. Region II includes friction coefficients that are larger than the converged friction coefficient and encompasses small geometric parameters (ρ<250). Due to the convergence of the frictional end with the clamped end, the critical buckling pressure in this region is solely dependent on the geometric parameter. The boundary value of ρ (ρ = 250) is determined based on the fluctuations in the critical pressure in the clamped end. When the geometric parameter exceeds this boundary value, the critical pressure for the spherical shell equates to that of a perfectly spherical one, as previously mentioned. As a result, the remaining region (region III) includes friction coefficients larger than the converged friction coefficient and geometric parameters greater than 250. The critical pressure in this region can be estimated using Eq. 1.

Table 3. Constants in the equation predicting the converged friction coefficient f_c

a	*b*	*c*
8.03	−0.16	−1.93

To explain the nonlinear relationship between the geometric parameter and the converged friction coefficient, as shown in Figure 7, the angle of rotation of the end edge φ should be examined. As indicated in Figure 8, the angle of rotation of the

end edge presents the degree of rotation from the initial state to the critical state of the end edge of the shell. Components of the reaction force at the top and bottom corners are also illustrated in Fig. 8 for further discussion. Because the length of the contact regions is relatively small compared to the thickness of the spherical shell, these reaction forces are treated as concentrated forces. In this figure, the subscripts "*t*" and "*b*" denote the components at the top and bottom corners, respectively. There exists a strong relationship between the reaction force components and the rotation angle of the end edge at the critical state, as depicted in Figure 8. The magnitude and direction of the reaction force components contribute to the formation of a resultant moment of force M_F. The characteristics of this resultant moment of force directly impact the rotation angle of the end edge; for instance, if this resultant moment of force is in an anticlockwise direction, the end edge rotates accordingly.

From the above definitions, the angle of rotation of the end edge is calculated at the critical pressure and illustrated in Figure 9. Since there is no rotation angle of the end edge in the clamped end, the frictional end converges with the clamped end as its angle of rotation approaches zero. For all geometric parameters, the frictionless end exhibits the highest angle of rotation. As the friction coefficient increases, the angle of rotation in the frictional end diminishes, eventually reaching zero at a certain value of the friction coefficient, corresponding to the converged friction coefficient. This trend is observable in Figure 9, where there is a gradual decrease in the angle of rotation at small geometric parameters. However, at larger ones, it demonstrates a rapid reduction as the friction coefficient increases. Notably, as the geometric parameter increases, the friction coefficient value at which the angle of rotation of the end edge vanishes nonlinearly decreases. In other words, the value of the friction coefficient at which the disappearance of the angle of rotation, as illustrated in Figure 9, aligns with the converged friction coefficient depicted in Figure 7.

Building on the categorization outlined in Fig. 7, the dependence of critical pressure on the friction coefficient and the geometric parameter varies. Therefore, the critical pressure must be predicted for each defined region. In region I, both the friction coefficient and the geometric parameter influence the critical pressure, as given by

$$\begin{aligned}\frac{p_{cr}}{p_0}\left(f_{ref},\rho_{ref}\right) &= a_1 + a_2\,\rho_{ref} + a_3 f_{ref} \\ &+ a_4\rho_{ref}^2 + a_5\rho_{ref}f_{ref} + a_6 f_{ref}^2 + a_7\rho_{ref}^2 f_{ref} \\ &+ a_8\rho_{ref}f_{ref}^2 + a_9\rho_{ref}^3 + a_{10}\rho_{ref}^2 f_{ref}^2 + a_{11}\rho_{ref}f_{ref}^3 \\ &+ a_{12}f_{ref}^4 + a_{13}\rho_{ref}^2 f_{ref}^3 + a_{14}\rho_{ref}f_{ref}^4 + a_{15}f_{ref}^5,\end{aligned} \tag{4}$$

where:

$$f_{ref} = \frac{f - 0.794}{0.615} \tag{5}$$

and

$$\rho_{ref} = \frac{\rho - 580.7}{1527} \tag{6}$$

$$\begin{cases} f < f_c \\ 8.6 \le \rho \le 8866.0 \end{cases} \tag{7}$$

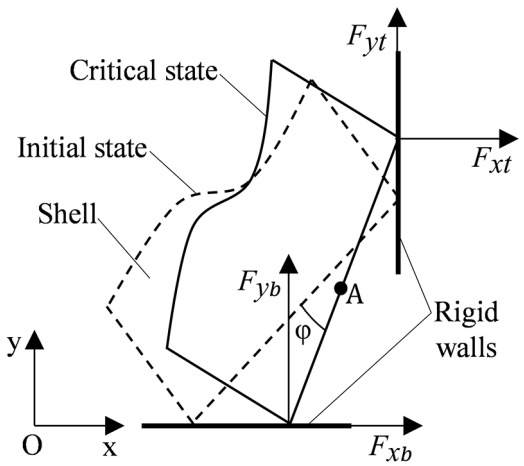

Fig. 8. Illustration of the angle of rotation of the end edge and components of reaction forces

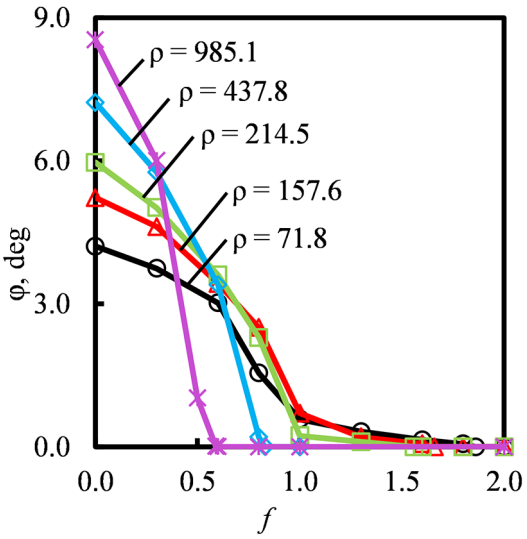

Fig. 9. Angle of rotation of the end edge at critical pressure for different geometric parameters

Table 4. Constants in the equation to predict the relative critical pressure in region I

a_1	a_2	a_3	a_4	a_5
1.001	−1.263	−0.607	−6.819	−7.096
a_6	a_7	a_8	a_9	a_{10}
−1.358	−13.060	−6.886	−0.384	−8.391
a_{11}	a_{12}	a_{13}	a_{14}	a_{15}
−1.425	0.109	−1.814	0.286	0.012

The relative critical pressure in this region can be estimated using Eq. 4 for each pair of the friction coefficient and geometric parameter, with an RMSE of 0.127. The constants a_i are determined using the linear least squares fitting method and are presented in Table 4. The valid boundary for the friction coefficient and geometric parameter in this region is constrained by Eq. 7. In region II, the critical pressure is solely a function of the geometric parameter and can be estimated using the following equation:

$$\frac{p_{cr}}{p_0}\left(\rho_{ref}\right) = b_1 + b_2\rho_{ref} + b_3\rho_{ref}^2 + b_4\rho_{ref}^3 + b_5\rho_{ref}^4 + b_6\rho_{ref}^5 + b_7\rho_{ref}^6 + b_8\rho_{ref}^7 + b_9\rho_{ref}^8 + b_{10}\rho_{ref}^9 \quad (8)$$

where:

$$\rho_{ref} = \frac{\rho - 132.2}{122.8} \quad (9)$$

$$\begin{cases} f \geq f_c \\ 8.6 \leq \rho \leq 250.0 \end{cases} \quad (10)$$

Equation 8 predicts the relative critical pressure with an RMSE of 0.071, and its constants b_i are listed in Table 5. Equation 8 applies to the valid boundary of the friction coefficient and geometric parameter, as indicated in Eq. 10. As indicated in Eq. 8 within the specified range from Eq. 10, each coefficient b_i is multiplied by a power function of the geometric parameter, except for the constant b_1. Consequently, variations in the relative critical pressure result from changes in geometric parameters affecting these coefficients, excluding b_i. Examining Eq. 8 without the geometric parameter's impact, the coefficient b_1 depends on the critical pressure of fully perfect spherical shells p_0. This critical pressure is a function of thickness, radius, and material properties, as expressed in Eq. 1. Hence, these parametric factors can play a significant role in influencing the value of the coefficient. Finally, the critical pressure in region III could be estimated by Eq. 1. The application of the friction coefficient and geometric parameter in this region is as follows:

$$\begin{cases} f \geq f_c \\ 250.0 < \rho \leq 8866.0 \end{cases} \quad (11)$$

Based on these predicted equations, a contour plot illustrating the dependence of critical pressure on the friction coefficient and geometric parameter is presented in Figure 10. The critical pressure nonlinearly increases with an increase in either the friction coefficient or geometric parameter and then it converges with that of the clamped end. The relationships depicted in this figure are consistent with those shown in Figure 6. As evident in Figure 10, region I exerts the most significant influence on critical pressure; even a minor alteration in the friction coefficient can result in a substantial change in critical pressure. In practical applications, for each geometric parameter, achieving a friction coefficient greater than the converged friction coefficient through the method of joining the end edge will increase the spherical shell's resistance to buckling.

To examine the effect of friction on the buckling deformation of the spherical shell, Figure 11 presents the distribution of radial displacement w_r at the critical pressure along the polar

Table 5. Constants in the equation to predict the relative critical pressure in region II

b_1	b_2	b_3	b_4	b_5
1.029	0.359	−2.588	−2.151	10.671
b_6	b_7	b_8	b_9	b_{10}
2.311	−13.983	1.332	5.587	−1.712

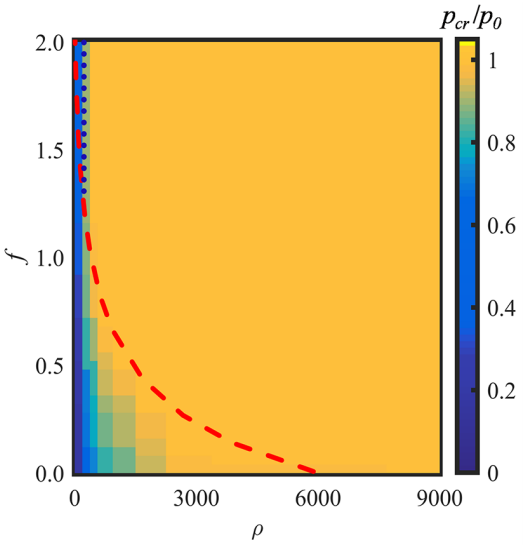

Fig. 10. Contour plot of the relative critical pressure

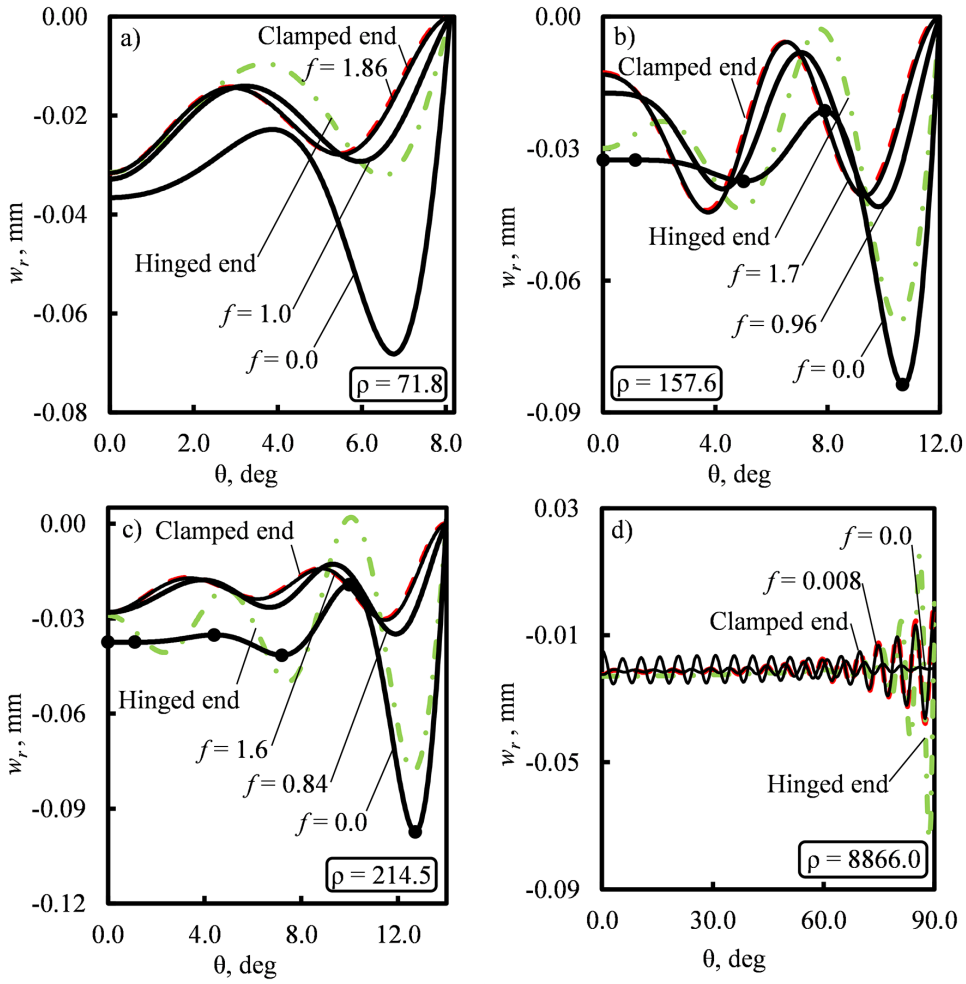

Fig. 11. Distribution of radial displacement along the polar angle at critical pressure for different geometric parameters with various end-edge boundary conditions

angle θ for different geometric parameters under clamped, hinged, and frictional ends. Initially, the mode of deformation, indicated by the number of extreme points, should be defined for discussion. Mode I has only one extreme point located at the center of the shell. Similarly, mode II exhibits two extremes: one at the center and another between the center and the edge. Higher modes can be defined using the same principle [11-13].

As observed in Figure 11, friction exerts a strong influence on the deflection of spherical shells, with the highest deformation occurring at the frictionless end. As the friction coefficient increases, buckling deformation decreases, eventually converging with that of the clamped end. For specific geometric parameters, such as ρ values of 157.6 and 214.5, an increase in the friction coefficient leads to a reduction in the buckling mode—from mode V at $f = 0.0$ to mode IV at $f = 0.96$ and from mode VI at $f = 0.0$ to mode V at $f = 0.84$, as shown in Figure 11b and 11c, respectively. Transitions to smaller buckling modes due to changes in the friction coefficient have also been observed for smaller geometric parameters [35].

Buckling modes and buckling mode transitions from mode I to mode VI due to changes in friction are illustrated in Figure 12a. The values of the friction coefficient at which these buckling mode transitions occur, termed transitional friction coefficients f_t, are marked by dashed ellipses. These transitional friction coefficients are selected and plotted against their corresponding geometric parameters, as shown in Figure 12b.

$$f_t = e\rho^g + h \tag{12}$$

Table 6. Constants in the equation estimating the transitional friction coefficient f_t

e	*g*	*h*
419.10	−2.11	0.91

$$\rho < 240.0 \quad (13)$$

The value of the transitional friction coefficient can be estimated using Eq. 12, with a root mean square error (RMSE) of 0.05. The constants e, g, and h are listed in Table 6. Eq. 13 indicates the boundary value of the geometric parameter applied in Eq. 12. As shown in Figure 12, at smaller geometric parameters, the buckling mode transition occurs at higher friction coefficients. The transitional friction coefficient decreases as the geometric parameter increases. To explain this phenomenon, reaction forces at the top and bottom corners, the resultant moment of force due to these reaction forces, and the bending stress should be considered.

The reaction forces in the horizontal direction F_{xt} and the vertical direction F_{yt} at the top corner, as well as in the horizontal direction F_{xb} and the vertical direction F_{yb} at the bottom corner for a specific geometric parameter at different values of the friction coefficient, as defined in Figure 8, are depicted in Figures 13a, b, c, and d, respectively. The corresponding horizontal resultant reaction force F_x and vertical resultant reaction force F_y are also presented in Figure 13e and f. Figure 13a–d reveals that, under identical external pressure, as the friction coefficient increases, the horizontal reaction force at the bottom corner increases while it decreases at the top corner. Furthermore, these horizontal reaction forces are negative. Consequently, their fluctuations at the top and bottom corners contribute to a change in the resultant moment of force. These variations in reaction force components, as the friction coefficient changes, align with those observed in a study on small geometric parameters [35].

Figure 14 depicts the resultant moment of force due to reaction forces at the critical pressure for distinct geometric parameters. This resultant moment of force is computed at the center point of the end edge (point A in Fig. 8) and corresponds to the bending moment at the end edge of the spherical shells. The resultant moment of force has a positive value in the anticlockwise direction and vice versa. The decrease, change in sign from positive to negative, and eventual increase in the resultant moment of force as the friction coefficient rises are consistent with the trends observed in the study on small geometric parameters [35]. This alteration in the resultant moment of force may influence the bending moment of the spherical shell.

The distribution of tangential stress σ_θ at the inner and outer surfaces of the spherical shell at the critical pressure is depicted in Figure 15a. The central portion of Figure 15a is highlighted in Figure 15b to indicate the movement of the no-bending point. This point corresponds to the polar angle θ_{NB} where the tangential stress at the inner surface is identical to that at the outer surface. As shown in Figure 14, the resultant moment of force changes as the friction coefficient increases. This alteration in the resultant moment of force leads to the movement of the no-bending point [35]. The shift of the no-bending point is influenced by the

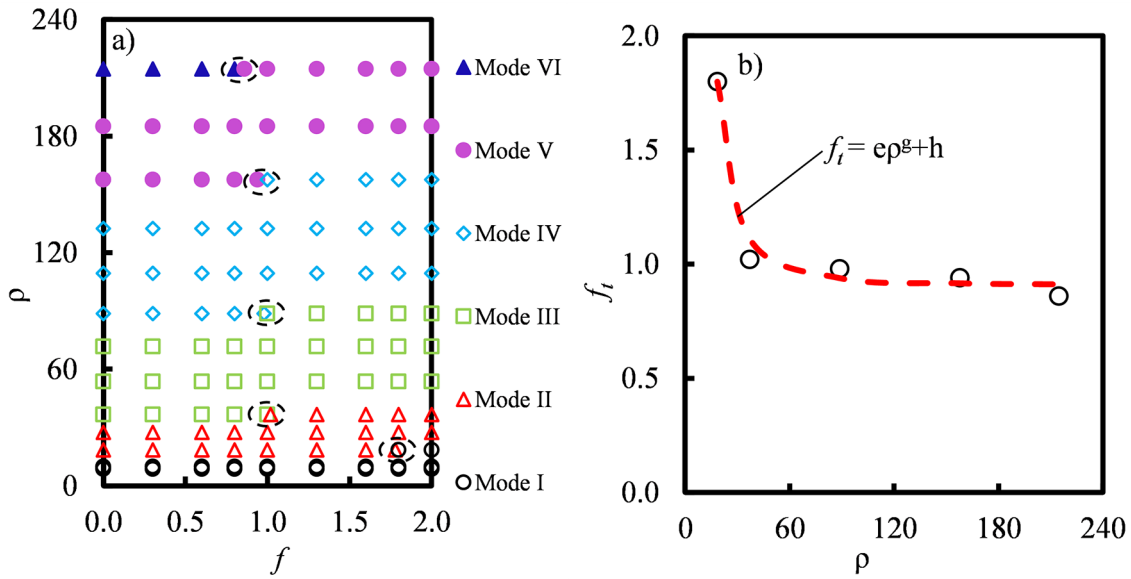

Fig. 12. (a) Buckling modes and (b) relationship between geometric parameter and friction coefficient for buckling mode transition

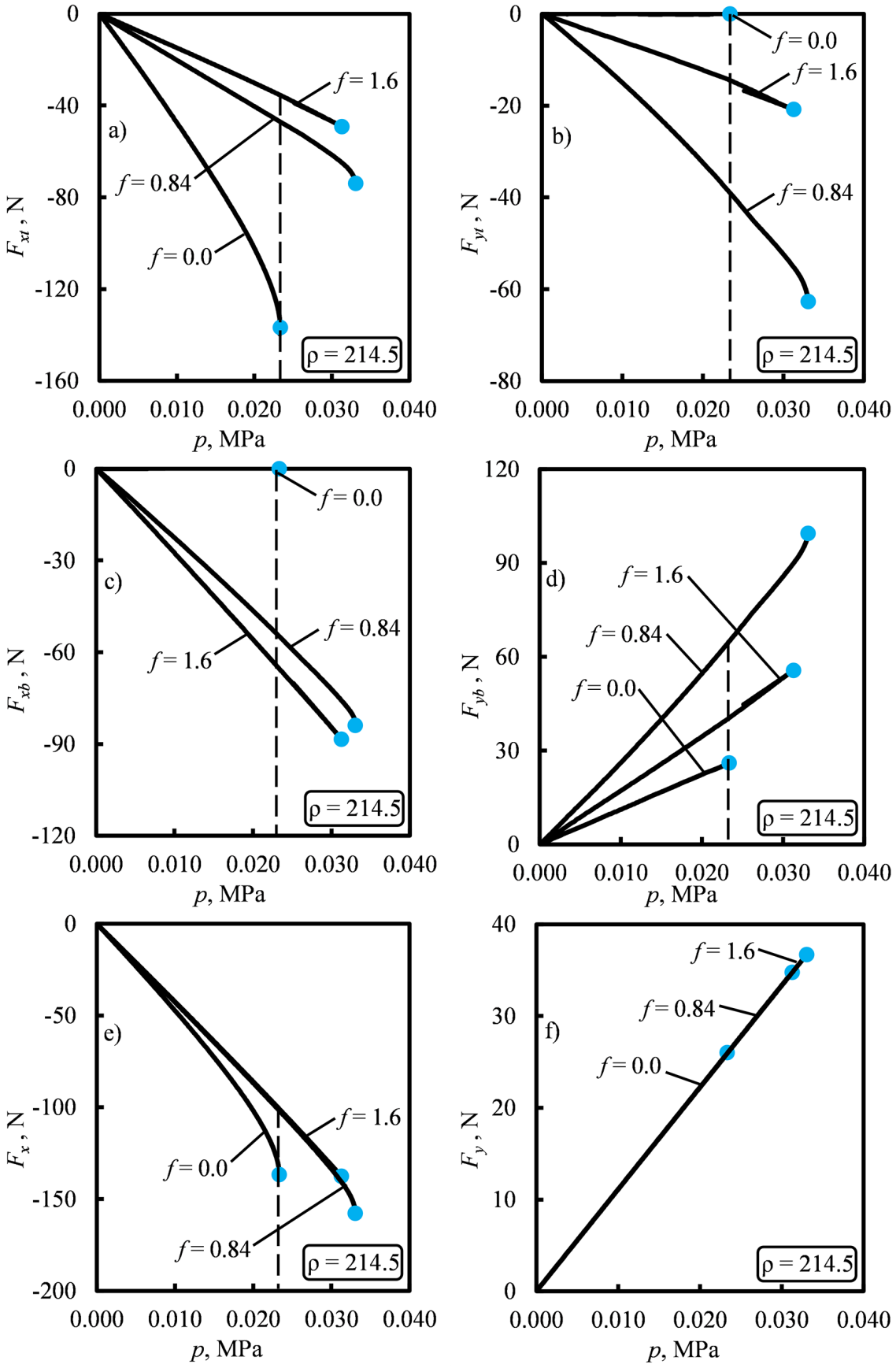

Fig. 13. (a) Horizontal reaction force and (b) vertical reaction force at the top corner; (c) horizontal reaction force and (d) vertical reaction force at the bottom corner; (e) horizontal resultant reaction force and (f) vertical resultant reaction force

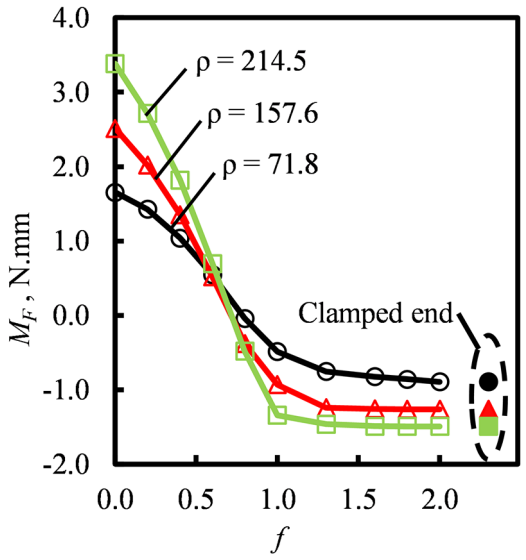

Fig. 14. Resultant moment of force due to the reaction forces at the critical pressure

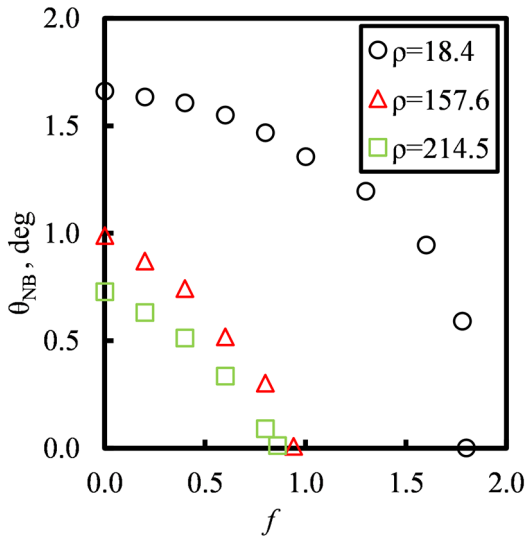

Fig. 16. Movement of the no-bending point for different geometric parameters

vertical and horizontal resultant forces F_y and F_x, as indicated in Figure 13f and 13e, respectively. The vertical resultant force maintains equilibrium with the external pressure, while the horizontal one primarily associates with the resultant moment of force. The external pressure generates a moment in an anticlockwise direction at the end edge while the direction of the resultant moment of force is opposite. Because the vertical resultant force is smaller than the horizontal resultant force, the resultant moment of force dominates over the moment due to the external pressure. As a result, the no-bending point shifts closer to the central portion. The shift of the no-bending point is continuous until it reaches the central area. Here, the bending moment is equal to zero. Consequently, the number of no-bending points decreases, leading to a change in the buckling mode. Therefore, the buckling mode transition occurs when the no-bending point reaches this central area [35].

The relationship between the friction coefficient and the location of the no-bending point is depicted in Figure 16. In a frictionless end, the larger the geometric parameter, the closer the

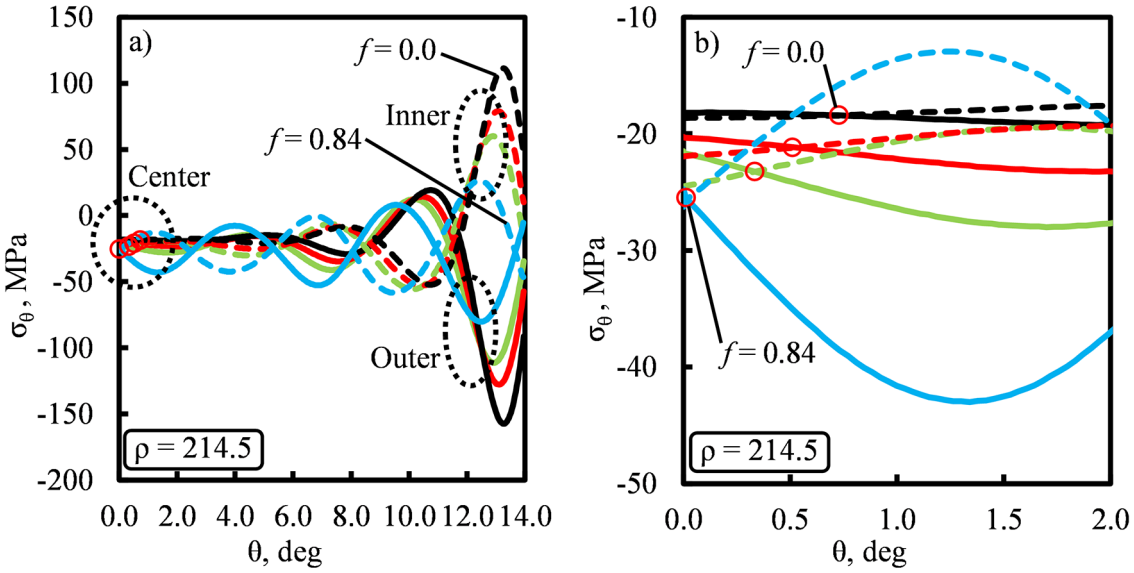

Fig. 15. (a) Distribution of tangential stress at the inner (dotted curves) and outer (solid curves) surfaces and (b) movement of the no-bending point at the critical pressure

no-bending point is to the center. As the friction coefficient increases, the no-bending point nonlinearly shifts toward the center. Additionally, at larger geometric parameters, the change in the theta angle of the no-bending point is more significant than at smaller ones when the friction coefficient increases. Therefore, the transitional friction coefficient is higher for smaller geometric parameters, as indicated in Figure 12.

CONCLUSIONS

This study examines the buckling behavior of thin, elastic spherical shells across a wide range of geometric parameters, from shallow to hemispherical shells, subjected to uniform external pressure. Three distinct types of boundary conditions for the end edge—clamped, hinged, and frictional ends—are considered to assess the influence of friction on the buckling performance of the shells. An axisymmetric finite element model is developed, and a nonlinear analysis technique is applied. The results reveal a significant impact of friction on the buckling behavior of spherical shells. Specifically, when the friction coefficient is smaller than the converged friction coefficient, reducing the friction coefficient renders the spherical shell more susceptible to buckling. A formula is derived to estimate this converged friction coefficient for each geometric parameter. This study also establishes a boundary that delineates the influence of friction on critical pressure in distinct regions. For each of these regions, an equation predicting the critical pressure is formulated. Moreover, the effect of friction on the buckling mode transition of the spherical shell is examined. Due to the more substantial change in the theta angle of the no-bending point at higher geometric parameters as the friction coefficient increases, buckling mode transitions occur at lower friction coefficients in wide spherical shells. From these findings, the results of this study hold potential applications in the design of spherical shells in marine industries and aerospace, particularly in understanding buckling failure. The limitation of this study is that it does not take into account initial imperfections, which are challenging to reproduce in experiments. For simplification, this study has focused on examining thin, elastic spherical shells without initial imperfections. Our focus is on the uniform external pressure loading condition. In the future, this investigation could be extended to the non–uniform loading scenarios or dynamics loads. In this study, the material is considered to be in the elastic region. Nevertheless, the elastic-plastic properties of materials can influence the buckling behavior of spherical shells. Furthermore, the potential influence of temperature could be a subject of further investigation.

Acknowledgment

This study was supported by the Ministry of Education, Science, Sports, and Culture of the Government of Japan.

REFERENCES

1. Zoelly R. About a buckling problem on the spherical shell (Üeber ein Knickungsproblem an der Kugelschale). Ph.D Thesis, ETH Zurich, Zurich 1915. doi: 10.3929/ethz-a-000091951
2. Kollar L. Buckling of complete spherical shells and spherical caps. In: Proceedings of a State-of-the-Art Colloqium, Berlin, Germany 1982, 401-425. doi: 10.1007/978-3-642-49334-8_14
3. Pan B.B., Cui W.C., Shen Y.S., Liu T. Further study on the ultimate strength analysis of spherical pressure hulls. Marine Structures 2010; 23(4): 444–461. doi: 10.1016/j.marstruc.2010.11.001
4. Pan B.B., Cui W.C., Shen Y.S. Experimental verification of the new ultimate strength equation of spherical pressure hulls. Marine Structures 2012; 29(1): 169–176. doi: 10.1016/j.marstruc.2012.05.007
5. Zhang J., Zhang M., Tang W., Wang W., Wang M. Buckling of spherical shells subjected to external pressure: A comparison of experimental and theoretical data. Thin-Walled Structures 2017; 111: 58–64. doi: 10.1016/j.tws.2016.11.012
6. Wagner H.N.R., Hühne C., Zhang J., Tang W., Khakimova R. Geometric imperfection and lower-bound analysis of spherical shells under external pressure. Thin-Walled Structures 2019; 143: 106195. doi: 10.1016/j.tws.2019.106195
7. Tsien H.S. A Theory for the buckling of thin shells. Journal of the Aeronautical Sciences 1942; 9(10): 373–384. doi: 10.1016/B978-0-12-398277-3.50011-7
8. Reissner E. Stresses and small displacements of shallow spherical shells. I. Studies in Applied Mathematics 1946; 25(1–4): 80–85. doi:10.1002/sapm194625180
9. Kaplan A., Fung Y.C. A nonlinear theory of bending and buckling of thin elastic shallow spherical shells. NACA Technical Note 3212, California Institute of Technology, Washington 1954, 1–58.

10. Litle W.A. Reliability of shell buckling predictions based upon experimental analysis of plastic models. Ph.D Thesis, Massachusetts Institute of Technology, the United States of America 1956.
11. Reiss E.L., Greenberg H.J., Keller H.B. Nonlinear deflections of shallow spherical shells. Journal of the Aeronautical Sciences 1957; 24(7): 533–543. doi: 10.2514/8.3893
12. Weinitschke H.J. On the nonlinear theory of shallow spherical shells. Journal of the Society for Industrial and Applied Mathematics 1958; 6(3): 209–232. doi: 10.1137/0106015
13. Reiss E.L. Axially symmetric buckling of shallow spherical shells under external pressure. Journal of Applied Mechanics 1958, 25(4): 556–560. doi: 10.1115/1.4011872
14. Keller H.B., Reiss E.L. Spherical cap snapping. Journal of the Aerospace Sciences 1959; 26(10): 643–652. doi: 10.2514/8.8240
15. Budiansky B. Buckling of clamped shallow spherical shells. Technical Report No.5, Harvard University, Massachusetts 1959, 1–48.
16. Homewood R.H., Brine A.C., Johnson A.E. Experimental investigation of the buckling instability of monocoque shells. Experimental Mechanics 1961; 1(3): 88–96. doi: 10.1007/BF02324071
17. Thurston G.A. A numerical solution of the nonlinear equations for axisymmetric bending of shallow spherical shells. Journal of Applied Mechanics 1961; 28(4): 557–562. doi: 10.1115/1.3641782
18. Archer R.R. On the numerical solution of the nonlinear equations for shell of revolution. Studied in Applied Mathematics 1962; 41(1–4): 165–178. doi:10.1080/21642583.2014.98634
19. Krenzke M.A., Kiernan T.J. Elastic stability of near-perfect shallow spherical shells. AIAA Journal 1963; 1(12): 2855–2857. doi: 10.2514/3.2187
20. Parmerter R.R. The buckling of clamped shallow spherical shells under uniform pressure. Ph.D Thesis, California Institute of Technology, the United States of America 1964. doi: 10.7907/R18G-ZC96
21. Archer R.R., Famili J. On the vibration and stability of finitely deformed shallow spherical shells. Journal of Applied Mechanics 1965; 32(1): 116–120. doi:10.1115/1.3625705
22. Thurston G.A., Penning F.A. Effect of axisymmetric imperfections on the buckling of spherical caps under uniform pressure. AIAA Journal 1966; 4(2): 319–327. doi: 10.2514/3.3435
23. Wang L.R.L. Discrepancy of experimental buckling pressures of spherical shells. AIAA Journal 1967; 5(2): 357–359. doi: 10.2514/3.3975
24. Sunakawa M., Ichida K. A high precision experiment on the buckling of spherical caps subjected to external pressure. ISAS report/Institute of Space and Aeronautical Science, University of Tokyo, Tokyo 1974, 87–121.
25. Yamada S., Uchiyama K., Yamada M. Experimental investigation of the buckling of shallow spherical shells. International Journal of Non-Linear Mechanics 1983; 18(1): 37–54. doi: 10.1016/0020-7462(83)90017-3
26. Grigolyuk E.I., Lopanitsyn Y.A. The axisymmetric postbuckling behaviour of shallow spherical domes. Journal of Applied Mathematics and Mechanics 2002; 66(4): 605–616. doi: 10.1016/S0021-8928(02)00079-5
27. Marcinowski J. Stability of relatively deep segments of spherical shells loaded by external pressure. Thin-Walled Structures 2007; 45(10–11): 906–910. doi: 10.1016/j.tws.2007.08.034
28. Kołodziej S., Marcinowski J. Experimental and numerical analyses of the buckling of steel, pressurized, spherical shells. Advances in Structural Engineering 2018; 21(16): 1–18. doi: 10.1177/1369433218774371
29. Kloppel V.K., Jungbluth O. Contribution to the buckling problem of thin-walled spherical shells. Experiments and Calibration formulas. (Beitrag zum Durchschlagproblem dunnwandiger Kugelschalen. Versuche und Bemessungsformeln). Der Stahlbau 1953; 22(6): 121–130.
30. Krenzke M.A. The elastic buckling strength of near-perfect deep spherical shells with ideal boundaries. Report 1713, David Taylor Model Basin, the United States of America 1963, 1–17.
31. Krenzke M.A., Kierman T.J. The effect of initial imperfections on the collapse strength of deep spherical shells. Report 1757, Structural Mechanics Laboratory, Department of the Navy, the United States of America 1965, 1–34.
32. Huang N.C. Unsymmetrical buckling of thin shallow spherical shells. Journal of Applied Mechanics 1964; 31(3): 447–457. doi: 10.1115/1.3629662
33. Holston A. Approximate analytical solutions of the finite-deflection equations for a shallow spherical shell. Journal of Applied Mechanics 1964; 34(1): 65–72. doi: 10.1115/1.3607670
34. Kai-Yuan Y., Wei-Ping S., Cleghorn W.L. Axisymmetric buckling of thin shallow circular spherical shells under uniform pressure for large values of geometric parameter λ. International Journal of Non-Linear Mechanics 1994; 29(4): 603–611. doi: 10.1016/0020-7462(94)90026-4
35. Nguyen X.C., Arai Y., Araki W. Effect of friction on the buckling behavior of shallow spherical shells contacting with rigid walls. Archive of Mechanical Engineering 2023 (under review).
36. Zhou F., Chen Z., Zheng C., Xu F., Hu Y., Hou S., Qin Z. Experimental and numerical buckling

failure analysis of acrylic hemispheres for application in neutrino detector. Engineering Failure Analysis 2017; 78: 147–160. doi: 10.1016/j.engfailanal.2017.03.017

37. Qu F., Jiang Z., Lu H. Effect of mesh on springback in 3D finite element analysis of flexible microrolling. Journal of Applied Mathematics 2015, 2015: 1–7. doi: 10.1155/2015/424131
38. Li L., Wang L., Etsion I., Talke F. The effect of contact conditions and material properties on plastic yield inception in a spherical shell compressed by a rigid flat. International Journal of Solids and Structures 2011; 48(3–4): 463–471. doi: 10.1016/j.ijsolstr.2010.10.015
39. Li L., Etsion I., Ovcharenko A., Talke F. The onset of plastic yielding in a spherical shell compressed by a rigid flat. Journal of Applied Mechanics 2011; 78(1): 011016. doi: 10.1115/1.4001994
40. Ronen S., Goltsberg R., Etsion I. A comparison of stick and slip contact conditions for a coated sphere compressed by a rigid flat. Friction 2017; 5(3): 326–338. doi: 10.1007/s40544-017-0178-2
41. Riks E. The application of Newton's method to the problem of elastic stability. Journal of Applied Mechanics 1972; 39(4): 1060–1065. doi: 10.1115/1.3422829
42. Riks E. An incremental approach to the solution of snapping and buckling problems. International Journal of Solids and Structures 1979; 15(7): 529–551. doi: 10.1016/0020-7683(79)90081-7
43. Riks E. Some computational aspects of the stability analysis of nonlinear structures. Computer Methods in Applied Mechanics and Engineering 1984; 47(3): 219–259. doi: 10.1016/0045-7825(84)90078-1
44. Shariati M., Allahbakhsh H.R. Numerical and experimental investigations on the buckling of steel semi-spherical shells under various loadings. Thin-Walled Structures 2010; 48(8): 620–628. doi: 10.1016/j.tws.2010.03.002
45. Nasto A., Reis P.M. Localized structures in indented shells: A numerical investigation. Journal of Applied Mechanics 2014; 81(12): 21008. doi: 10.1115/1.4028804
46. Lee A., Jiménez F.L., Marthelot J., Hutchinson J.W., Reis P.M. The geometric role of precisely engineered imperfections on the critical buckling load of spherical elastic shells. Journal of Applied Mechanics 2016; 83(11): 11005. doi: 10.1115/1.4034431
47. Wang Y., Tang W., Zhang J., Zhang S., Chen Y. Buckling of imperfect spherical caps with fixed boundary under uniform external pressure. Marine Structures 2019; 65: 1–11. doi: 10.1016/j.marstruc.2019.01.004
48. Wang Y., Zhang J., Tang W. Buckling performances of spherical caps under uniform external pressure. Journal of Marine Science and Application 2020; 19(1): 96–100. doi: 10.1007/s11804-020-00125-7
49. Jasion P., Magnucki K. Elastic buckling of barrelled shell under external pressure. Thin-Walled Structures 2007; 45(4): 393–399. doi: 10.1016/j.tws.2007.04.001
50. Archer R.R. Stability limits for a clamped spherical shell segment under uniform pressure. Quarterly of Applied Mathematics 1958; 15(4): 355–366. doi: 10.1090/qam/98515